1 **The role of dust mineral composition in atmospheric radiation and pollution in North**
2 **China: new insights from EMIT and two-way coupled modeling**
3

4 Chao Gao[1], Xuelei Zhang[1, 2, *], Hu Yang[1], Ling Huang[3], Hongmei Zhao[1], Shichun Zhang[1], and Aijun Xiu[1]
5
6 [1]State Key Laboratory of Black Soils Conservation and Utilization, Northeast Institute of Geography and Agroecology,
7 Chinese Academy of Sciences, Changchun, 130102, China
8 [2]School of Geographical Sciences, Liaoning Normal University, Dalian, 116029, China
9 [3]School of Environmental and Chemical Engineering, Shanghai University, Shanghai 200444, China
10 [*]Correspondence to: X.L. Zhang (zhangxuelei@neigae.ac.cn)
11

12 **Abstract**

13   Mineral dust is a major atmospheric aerosol influencing Earth's energy balance

14 through aerosol-radiation (ARI) and aerosol-cloud interactions (ACI). While homogeneous

15 dust effects have been studied, the impact of mineralogical composition on regional

16 meteorology and air quality remains underexplored, limiting accurate forecasting of dust

17 storm impacts, especially in dust belt regions. In this study, we used a two-way coupled

18 WRF-CHIMERE model with three mineralogical dust atlases (Nickovic et al. (2012)

19 (N2012), Journet et al. (2014) (J2014), and a new dataset, Li et al. (2024) (L2024), from

20 the Earth Surface Mineral Dust Source Investigation (EMIT)) to evaluate ARI effects

21 during the March 2021 dust storm in North China. Results showed significant spatial

22 variations in radiative forcing due to mineralogical differences. Bulk dust (without

23 considering mineralogy) caused an average shortwave radiative forcing of -5.72 W/m²,

24 while mineral-specific forcings increased this by up to $+0.10$ W/m². Integrating EMIT data

25 reduced PM_{10} biases by over 15% in high-concentration regions and improved ozone

26 predictions, with localized changes of -2.46 to $+3.52$ μg/m³. Hematite's strong absorption

27 and quartz's reflective properties were key in altering radiative and air quality outcomes.

28 Compared to scenarios of bulk dust, the consideration of ARI effects of mineralogical

29 compositions can increase PM_{10} concentration by up to 1189.48 μg/m³ in dust source

30 regions. Future research perspectives on the utilization of high-resolution EMIT data in

31 two-way coupled meteorology and air quality models for investigating the ACI effects of

mineralogical dust on cloud microphysics are proposed.

1 Introduction

Mineral dust, a dominant component of global atmospheric aerosols, primarily originates from wind erosion in arid and semi-arid regions (Schepanski, 2018; Shao et al., 2011). It can affect the Earth's energy balance through direct scattering and absorption of solar, i.e. aerosol-radiation interaction (ARI), as well as indirect effects on cloud properties by acting as cloud condensation nuclei and ice nuclei, i.e., aerosol-cloud interaction (ACI) (Choobari et al., 2014; Kok et al., 2023). By altering biogeochemical cycles, atmospheric chemistry and visibility, and air quality, transported mineral dust can exacerbate economic losses, and health risks (Adebiyi et al., 2023; Cwiertny et al., 2008; Duniway et al., 2019; Maher et al., 2010; Tong et al., 2023). Accurate forecasting of mineral dust events is crucial to mitigate these adverse impacts.

Numerous studies have demonstrated that the magnitude of dust ARI and ACI effects is significantly influenced by its mineralogical composition. For instance, iron oxides, particularly hematite and goethite, have been identified as key components responsible for dust absorption of solar radiation, as evidenced by both observational and modeling studies (Alfaro et al., 2004; Gómez Maqueo Anaya et al., 2024; Lafon et al., 2006; Li et al., 2022; Obiso et al., 2024; Scanza et al., 2015; Song et al., 2024). Concurrently, a growing body of research has explored the impact of various dust mineral compositions, including hematite, corundum, kaolinite, muscovite, montmorillonite, quartz, calcite, illite, amorphous silicon, aluminum silicate, and potassium feldspar, on ice nucleation processes. Among these, potassium feldspar has emerged as a crucial component for dust nucleation activation (Harrison et al., 2016; Kumar et al., 2018). However, a notable gap exists in our understanding of how specific mineral compositions impact meteorology and air quality through ARI and ACI effects. Prior research has predominantly focused on homogeneous dust aerosols, assuming globally uniform composition and optical properties. However, this assumption introduces regional inaccuracies in estimating the impacts of dust aerosols,

59   which remain poorly understood due to uncertainties in dust composition (Ke et al., 2022;

60   Klingmüller et al., 2019; Kok et al., 2017).

61   Many efforts have been directed to improve simulations of dust mineralogy and its

62   representation in numerical models (Balkanski et al., 2021; Gómez Maqueo Anaya et al.,

63   2024; Gonçalves Ageitos et al., 2023; Li et al., 2021, 2022, 2024; Li and Sokolik, 2018;

64   Menut et al., 2020; Obiso et al., 2024; Scanza et al., 2015; Solomos et al., 2023b, a; Song

65   et al., 2024). Most of the above are offline models, with only two studies conducting two-

66   way feedback simulations with only WRF-Chem (Li and Sokolik, 2018) and WRF-

67   CHIMERE (Menut et al., 2020) being applied. However, both of these studies are derived

68   from artificially generated data and lack effective ground-based validation, as discussed in

69   Claquin et al. (1999), Nickovic et al. (2012) (N2012 hereafter), and Journet et al. (2014)

70   (J2014 hereafter). These validations predominantly focus on agricultural regions rather

71   than the arid and semi-arid areas that are major sources of dust emissions (Green et al.,

72   2020). EMIT instrument provides a new approach to invert and obtain the surface soil

73   mineral composition and further assess the ARI and ACI effects of dust minerals (Connelly

74   et al., 2021). To the best of our knowledge, no prior research has investigated the impact

75   of dust on regional meteorology and air quality while considering its mineral speciation

76   using two-way coupled models with three different mineralogical dust atlases.

77   Due to the nucleation mechanism of aeolian mineral components (ACI effect) not

78   being incorporated into the two-way coupled model, this study utilizes a two-way coupled

79   WRF-CHIMERE model incorporating three mineral databases to explore how dust particle

80   mineral composition interacts with radiation and North China during a heavy dust storm

81   event. The following sections detail the methodology (model configurations and data

82   sources) in Section 2, analyze the WRF-CHIMERE simulations focusing on ARI effects of

83   dust mineral composition on meteorology and air quality in Section 3, and summarize the

84   key findings in Section 4.

85

86

2 Methodology and data

2.1 Model configurations and data sources

The two-way coupled WRF model version 3.7.1 and CHIMERE model version 2020r3 were employed to simulate the ARI and ACI effects of mineralogical dust particles on meteorology and air quality over North China from March 12 to March 15, 2021, as shown in Fig. A1. The exchanges between meteorological and air quality variable are accomplished through the OASIS coupler (Briant et al., 2017). The simulation was conducted at a horizontal resolution of 27 km, with 165 grid cells in the east-west direction and 87 in the north-south direction, and the study domain is depicted in Fig. A1. The model has 33 vertical levels from surface to 50 hPa with 13 layers in the bottom 1km and the bottom thickness being 24.5 m. The Rapid Radiative Transfer Model for General circulation models (RRTMG) shortwave and longwave radiation schemes were employed to investigate the ARI effects (Briant et al., 2017). Additionally, the Thompson cloud microphysics scheme was utilized to assess the impacts of ACI (Tuccella et al., 2019). The initial and boundary conditions (ICs and BCs) for non-dust aerosols are prescribed by the LDMZ-INCA model, while those for dust aerosols are determined by the GOCART model. The options of other physics and chemistry schemes are presented in Table A1. The dry depositions are treated as described in Zhang et al. (2001). The parameterizations for the removal of dust particles below clouds by raindrops and snow are based on the methods proposed by Willis & Tattelman (1989) and Wang et al. (2014), respectively. Inline mineral dust emissions, incorporating mineralogy, are computed using a u* threshold and a dust production model for saltation (Kok et al., 2014; Shao and Lu, 2000). The model accounts for the impact of soil moisture on suppressing mineral dust emissions (Fécan et al., 1998).

For the calculations of ARI effects in WRF-CHIMERE, refractive indices corresponding to these mineralogical species are provided in Table 2 of Menut et al. (2020). Concerning shortwave (SW) radiation, the aerosol optical properties, encompassing single scattering albedos and asymmetry factors at 400 and 600 nm, as well as the aerosol optical depth (AOD) at 300, 400, and 999 nm, calculated using Fast-JX, were interpolated or

115 extrapolated to obtain values at 14 SW intervals (Briant et al., 2017; Gao et al., 2022). AOD

116 at 16 longwave (LW) intervals ranging from 3400 to 55600 nm are directly used to

117 calculate LW radiation.

118   To evaluate the model performance of the WRF-CHIMERE model with and without

119 including mineralogical dust emissions, we collected 132 hourly national environmental

120 observations for $PM_{2.5}$ and PM_{10} concentrations at https://quotsoft.net/air/. The shortwave

121 radiation (SSR) data, consisting of 59 hourly surface measurements, was sourced from

122 Tang et al. (2019). The 844 hourly surface meteorology station data can be accessed at

123 https://data.cma.cn.

124

125 **2.2 Mineral dust atlases**

126   Detailed soil composition data is crucial for separating the emission flux into

127 contributions from individual minerals. Mineral density and refractive index data are

128 referenced from Menut et al. (2020). Several global mineralogical composition databases

129 (N2012, J2014, EMIT) provide data on 12 mineral species (Table 1) at varying resolutions

130 (1 km × 1 km, 0.5° × 0.5°). These data are interpolated to match the study's model grid.

131 For consistency, the N2012 data (originally at 1 km × 1 km, accessible at

132 http://www.seevccc.rs/GMINER30) is resampled to 0.5° × 0.5°. The J2014 data,

133 implemented in the WRF-CHIMERE model, includes 12 mineral compositions found in

134 clay and/or silt fractions (details in Table 2 of Menut et al., 2020). EMIT data

135 (https://earth.jpl.nasa.gov/emit/data/data-products) requires specific processing. Since it

136 provides only normalized spectral abundance, it needs recalculation to represent the

137 normalized mass proportion of each mineral in each substrate. Additionally, EMIT lacks

138 data for feldspar and quartz. In cases where the total EMIT composition suggests less than

139 100% (indicating a missing mineral contribution), the missing fraction is filled to represent

140 the relative amounts of quartz and feldspar. As EMIT only combines illite and muscovite,

141 their individual contents are estimated based on the respective proportions in N2012 or

142 J2014 data. Regarding specific mineralogical species appear in both clay and silt soil

143 fractions, the contents of these species for EMIT dataset are calculated based on contents

144 of respective species in clay and silt soil for N2012 or J2014 datasets. The detailed

145 calculation steps can be found at https://earth.jpl.nasa.gov/emit/internal_resources/284.

146

147   Table 1. Mineralogical compositions in different datasets.

Mineral	Clay		Silt		EMIT
	N2012	J2014	N2012	J2014	
Smectite	✓	✓	✗	✗	✓
Illite	✓	✓	✗	✗	✓†
Hematite	✓	✓	✓	✗	✓
Feldspar	✗	✓	✓	✓	✗
Kaolinite	✓	✓	✗	✗	✓
Calcite	✓	✓	✓	✓	✓
Quartz	✓	✓	✓	✓	✗
Gypsum	✗	✗	✓	✓	✓
Vermiculite	✗	✓	✗	✗	✓
Chlorite	✗	✓	✗	✓	✓
Goethite	✗	✗	✗	✓	✓
Mica	✗	✗	✗	✓	✓†
Resolution	1km	0.5°	1km	0.5°	0.5°

148   † indicates the content of illite + muscovite

149

150 **2.3 Scenario set up**

151   Ten parallel WRF-CHIMERE simulations were performed to investigate the influence

152 of mineralogical dust on meteorology and air quality in China, employing three distinct

153 mineralogical atlases, as illustrated in Figs. 1 and A5-A7. Each simulation was conducted

154 both with and without enabling ARI effects, as detailed in Table 2, to isolate and compare

155 the effects of mineralogical dust under different modeling conditions.

156   Simulations without ARI effects (Dust_NO, N2012_default_NO, N2012_EMIT_NO,

157 J2014_default_NO, J2014_EMIT_NO) were specifically designed to identify the direct

158 impact of mineralogical dust on meteorology and air quality, independent of the radiative

159 feedbacks induced by aerosols. These No_ARI simulations served as a baseline for
160 assessing how mineralogical compositions affect meteorology and air quality in the
161 absence of aerosol-radiation feedback mechanisms.

162 In contrast, simulations with ARI enabled (Dust_ARI, N2012_default_ARI,
163 N2012_EMIT_ARI, J2014_default_ARI, J2014_EMIT_ARI) were used to quantify the
164 additional effects arising from aerosol-radiation interactions. By comparing simulations
165 with and without ARI for each mineralogical atlas (e.g., N2012_default_ARI −
166 N2012_default_NO), the differential impact of ARI effects on meteorology and air quality
167 for various dust compositions could be identified. This approach highlights how
168 mineralogical properties of dust influence the strength and nature of ARI effects, thereby
169 modulating key atmospheric processes such as radiation balance, temperature profiles, and
170 pollutant distributions.

171 To evaluate the discrepancies in ARI effects among the mineralogical atlases,
172 differences in the ARI impacts between EMIT-derived and default dust compositions were
173 analyzed for both N2012 and J2014 datasets. For example, comparisons such as
174 (N2012_EMIT_ARI − N2012_EMIT_NO) versus (N2012_default_ARI −
175 N2012_default_NO) provide insight into the extent to which higher-resolution, satellite-
176 derived mineralogical data influence ARI effects relative to default atlas-based
177 representations. Similar comparisons were performed for the J2014 dataset.
178
179
180
181
182
183
184
185
186
187
188
189
190

191   Table 2. Summary of dust emission scenarios and aerosol feedback configurations for
192   different simulation settings.

Scenario	Emission	Online choice	Coupling type	Aerosol feedback
Dust_NO	Bulk dust + anthropogenic emissions	[online] = 1	[cpl_case] = 1	No feedbacks
Dust_ARI		[online] = 1	[cpl_case] = 2	ARI effects
N2012_default_NO	N2012_default dust + anthropogenic emissions	[online] = 1	[cpl_case] = 1	No feedbacks
N2012_default_ARI		[online] = 1	[cpl_case] = 2	ARI effects
N2012_EMIT_NO	N2012_EMIT dust + anthropogenic emissions	[online] = 1	[cpl_case] = 1	No feedbacks
N2012_EMIT_ARI		[online] = 1	[cpl_case] = 2	ARI effects
J2014_default_NO	J2014_default dust + anthropogenic emissions	[online] = 1	[cpl_case] = 1	No feedbacks
J2014_default_ARI		[online] = 1	[cpl_case] = 2	ARI effects
J2014_EMIT_NO	J2014_EMIT dust + anthropogenic emissions	[online] = 1	[cpl_case] = 1	No feedbacks
J2014_EMIT_ARI		[online] = 1	[cpl_case] = 2	ARI effects

193
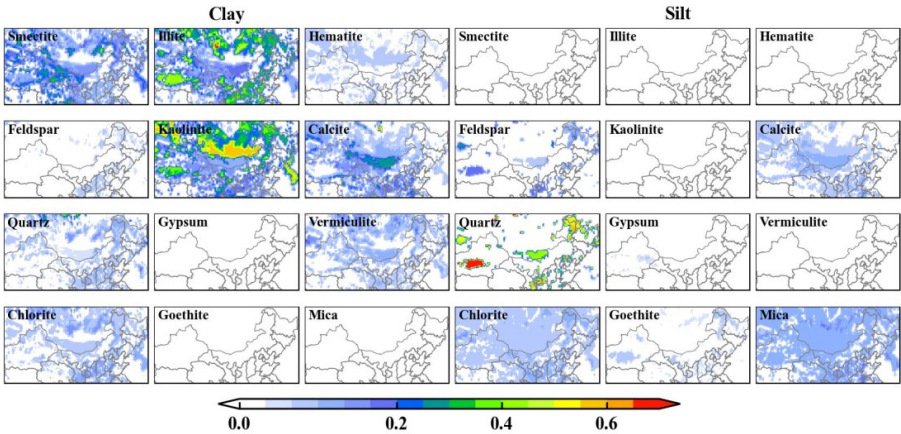
195   Figure 1. Spatial distribution of content for the different mineral dust species in the silt and clay fraction
196   of the soil for original J2014 mineralogical data.
197

3   Results and discussion

3.1 Evaluation of meteorology and air quality

200   Table 3 presents the evaluation results for observed and simulated surface shortwave

201   radiation (SSR), 2-meter temperature (T2), and 10-meter wind speed (WS10) from various

202   scenario simulations conducted using the WRF-CHIMERE modeling system. The model

203   exhibits strong overall performance, with correlation coefficients (R) between observed

204   and simulated values reaching approximately 0.7 for SSR and WS10, and up to 0.93 for

205   T2. These results demonstrate the model's capacity to capture key atmospheric patterns and

206   variability across the simulation domain. However, systematic biases are evident,

207   particularly in North China, where the model tends to overestimate SSR and WS10 by

208   60.69%–68.92% and 17.06%–17.52%, respectively, while underestimating T2 by 0.48%–

209   0.58%. These biases suggest challenges in accurately simulating surface radiation fluxes,

210   near-surface wind dynamics, and temperature fields, especially in areas influenced by high

211   aerosol concentrations.

212   A comparative analysis of the two configurations, N2012 and J2014, reveals that

213   WRF-CHIMERE with N2012 generally outperforms J2014 in simulating SSR and T2,

214   suggesting that the N2012 parameterization better captures radiative and thermodynamic

215   processes in the region. Conversely, J2014 exhibits improved accuracy in simulating WS10,

216   implying potential strengths in its representation of near-surface wind dynamics. These

217   findings highlight the sensitivity of model performance to parameterization schemes and

218   the need for tailored configurations for specific meteorological variables. The inclusion of

219   detailed dust mineralogical compositions, while informative for certain applications,

220   introduces additional complexities that reduce the overall accuracy of simulations.

221   Specifically, while these compositions help mitigate the overestimation of SSR and the

222   underestimation of T2, they exacerbate the overestimation of WS10. The integration of

223   EMIT satellite data provides a significant boost to model performance, highlighting the

224   value of incorporating high-resolution, real-time observational data to refine the simulation

225   of atmospheric variables. EMIT data, with its detailed characterization of aerosol and dust

226   properties, reduces the positive biases in SSR and WS10 while simultaneously minimizing

227   the negative biases in T2.

228   When comparing the ARI (aerosol-radiation interaction) effects of the defaulted

229   mineralogical compositions in N2012 and J2014 with simulations that implement EMIT

230   satellite data, the latter shows a clear advantage. Incorporating EMIT data further reduces

231   the positive biases in SSR and WS10, while simultaneously minimizing the negative biases

232 in T2. This suggests that EMIT data provides a more precise representation of dust

233 properties and atmospheric conditions, enhancing the overall reliability of the model.

234

235 Table 3. Statistics analysis of daily averaged SSR, 2-meter temperature (T2) and 10-meter wind speed
236 (WS10) from different scenario simulations and ground observations in North China including
237 correlation coefficient (R) and normalized mean bias (NMB).

Scenario	SSR		T2		WS10	
	R	NMB	R	NMB	R	NMB
Dust_NO	0.7041	68.92	0.9327	−0.5816	0.7112	17.0623
Dust_ARI	0.7170	60.69	0.9372	−0.4831	0.7178	17.4558
N2012_default_NO	0.7041	68.92	0.9327	−0.5816	0.7112	17.0623
N2012_default_ARI	0.7147	61.80	0.9369	−0.4758	0.7170	17.5280
N2012_EMIT_NO	0.7041	68.92	0.9327	−0.5816	0.7112	17.0623
N2012_EMIT_ARI	0.7161	60.88	0.9367	−0.4799	0.7174	17.4403
J2014_default_NO	0.7041	68.92	0.9327	−0.5816	0.7112	17.0623
J2014_default_ARI	0.7148	61.68	0.9368	−0.4779	0.7170	17.5096
J2014_EMIT_NO	0.7041	68.92	0.9327	−0.5816	0.7112	17.0623
J2014_EMIT_ARI	0.7154	61.22	0.9367	−0.4796	0.7174	17.4791

238

239 To assess the ability of each scenario simulation to replicate regional PM_{10} and O_3

240 temporal patterns, Figure 2 presents hourly time series of simulated and in situ PM_{10} and

241 O_3 concentrations at four North China sites: Ordos, Kalgan, Beijing, and Tianjin. These

242 locations represent key dust aerosol transport pathways, which play a crucial role in the

243 region's air quality dynamics due to frequent dust storms and anthropogenic emissions. The

244 time series plots regarding PM_{10} and O_3 in Figures 2 and A2 allow for a direct comparison

245 of model simulations with observed data, revealing important insights into model

246 performance across different environmental conditions and geographical settings,

247 respectively. All models accurately captured the peak PM_{10} and O_3 concentrations observed

248 during the March 12 event in North China, which was characterized by significant dust

249 emissions and high pollutant levels. This event serves as a key test case for evaluating the

250 models' responsiveness to extreme atmospheric conditions. However, despite the overall

251 agreement in peak concentration timings, simulations often overestimated O_3 and

252 underestimated PM_{10} at sites with high dust loads, such as Ordos and Kalgan. This

253   discrepancy highlights the challenge of simulating the complex interactions between dust

254   aerosols, precursor gases, and photochemical reactions, particularly in regions with high

255   dust deposition and frequent air pollution episodes. Additionally, the models tended to

256   extend the period of elevated PM_{10} concentrations beyond the observed time frame,

257   suggesting that the processes controlling dust aerosol removal or dispersion were not fully

258   captured. CHIMERE simulations using J2014 mineralogical data generally outperformed

259   those using J2012 data, with significant reductions in PM_{10} negative normalized mean

260   biases (NMBs) for three of the four cities, indicating the importance of accurate

261   mineralogical characterization of dust for improving model predictions. When considering

262   the aerosol-radiation interaction (ARI) effects of bulk dust aerosols, PM_{10} negative biases

263   decreased, and O_3 positive biases increased, which suggests that incorporating ARI effects

264   helps to better represent the impact of dust on local radiative forcing and air quality.

265   Moreover, incorporating ARI effects from the default dust mineralogical atlas further

266   enhanced these trends, underscoring the need for refined aerosol property data in enhancing

267   model performance. Finally, using Earth-observing systems such as the EMIT satellite data

268   led to substantial reductions in PM_{10} negative bias at Kalgan, Beijing, and Tianjin,

269   demonstrating the value of remote sensing data in improving model accuracy, particularly

270   for regions with high aerosol concentrations and complex emission sources.
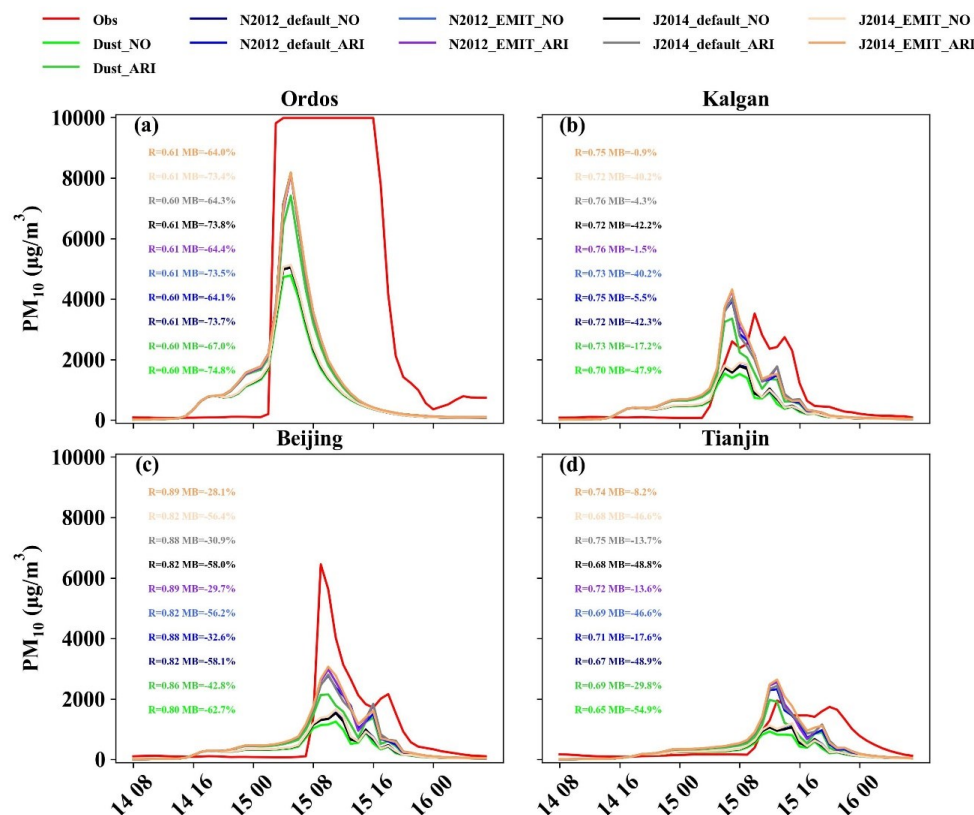
271

272

Figure 2. Statatiscal metrices between observed and simulated PM_{10} concentrations by different scenario simulations.

To evaluate the model performance in simulating the horizontal distribution and vertical profile of dust aerosol, Figure 3 presents the false RGB imagery of dust derived from Himawari-8 thermal infrared imagery, along with CALIPSO cross sections of 532 nm total attenuated backscatter and the vertical feature mask for the overpass of China. The figure also includes the corresponding spatial distributions of PM_{10} concentrations at 05:00 UTC on 15th March 2021, a time of significant dust transport in the region. This detailed comparison allows for a comprehensive assessment of how well the model captures both the horizontal and vertical characteristics of dust aerosol distribution. All six experiments show similar dust locations in the atmosphere, which are consistent with the Himawari-8

286 and CALIPSO observations, suggesting that the models effectively replicate the general

287 spatial patterns of dust transport. Specifically, the false RGB imagery from Himawari-8

288 clearly indicates the presence of dust plumes in the atmosphere, with distinct thermal

289 contrasts that help identify the dust layers. The CALIPSO data, which provide vertical

290 profiles of aerosol backscatter, further validate the model's ability to capture the vertical

291 extent and concentration of dust layers. These observations are critical for understanding

292 the atmospheric processes governing dust dispersion and their impact on air quality. The

293 close agreement between model simulations and satellite data across all six experiments

294 also underscores the robustness of the model in representing dust aerosol distribution under

295 different simulation conditions. This evaluation demonstrates that the models are capable

296 of simulating the main features of dust aerosol transport, though further refinement in

297 capturing the fine-scale variations and aerosol properties may still be necessary for more

298 accurate predictions in future studies.
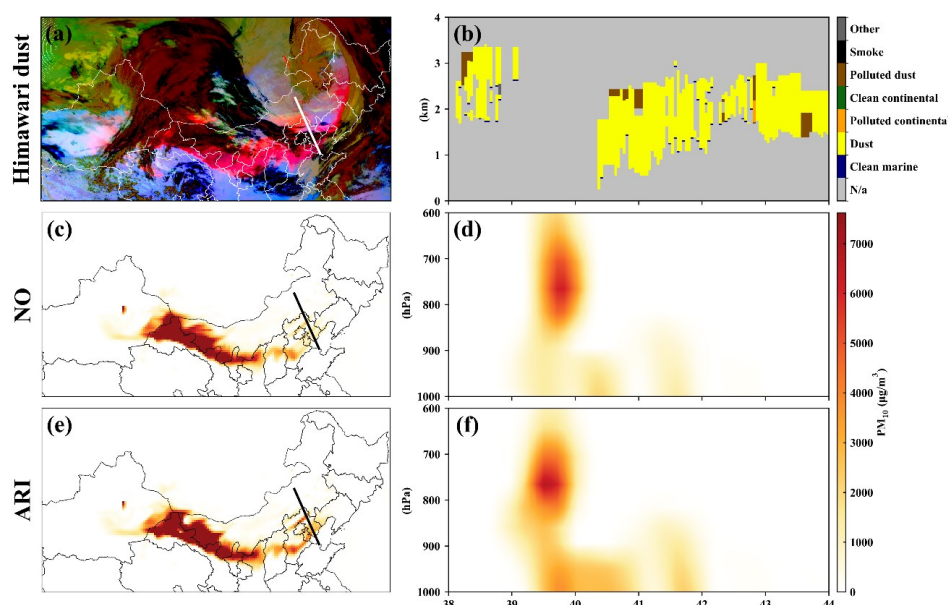
299

300 Figure 3. The false color imagery of dust from Himawari-8 thermal infrared imagery(a), CALIPSO

301 cross sections of 532 nm total attenuated backscatter and the vertical feature mask for the overpass of

302 China on 13:00 (local time) 15th March 2021 (b), and corresponding horizontal (c and e) and vertical (d

303 and f) distributions of PM_{10} concentrations.

3.2 Radiative effect on meteorology

304

305 To further investigate the impacts of dust radiation on energy balance, the spatial

306 distributions of the average shortwave (SW), longwave (LW), and net (NET) radiative

307 forcing induced by bulk dust on the surface (SFC), in the atmosphere (ATM), and at the

308 top of the atmosphere (TOA) are presented during the dust episode shown in Figure 4. The

309 radiative forcing values provide critical insights into the energy exchanges between dust

310 aerosols and the atmosphere, and their subsequent effects on regional climate dynamics.

311 For SW radiation forcings, dust aerosols produced cooling effects at all three layers: the

312 surface, the atmosphere, and the top of the atmosphere. The average SW radiative forcing

313 was about -5.72 W m^{-2} at the surface, -8.69 W m^{-2} in the atmosphere, and -2.97 W m^{-2}

314 at the TOA, highlighting the significant reduction in solar radiation reaching these layers

315 due to the scattering and absorption properties of the dust particles. Particularly in the dust

316 source regions, the cooling effect at the surface exceeded -900 W m^{-2} (Figures 4a, 4d, and

317 4g), indicating the strong influence of dust on the regional energy budget in these areas.

318 This is a result of the large dust concentrations and their optical properties, which

319 effectively block solar radiation from reaching the Earth's surface. In contrast, the dust-

320 induced LW radiative forcing warmed the surface and atmosphere, with average values

321 ranging from 5.78 to 5.86 W m^{-2}. This warming effect is associated with the absorption of

322 longwave radiation by dust particles, which then re-radiate heat, contributing to local

323 warming. However, dust particles induced negative LW radiative forcing at the TOA, with

324 values ranging from -461.88 to -379.95 W m^{-2}, reflecting the downward flux of longwave

325 radiation absorbed by the aerosols, which reduces the amount of energy reaching the TOA.

326 The NET radiative forcing, which represents the combined effect of both SW and LW

327 forcings, was positive at the surface (about $+0.15$ W m^{-2}), negative in the atmosphere

328 (about -2.91 W m^{-2}), and negative at the TOA (about -3.06 W m^{-2}), as shown in Figures

329 4c, 4f, and 4i. The positive NET radiative forcing at the surface suggests a slight net

330 warming effect at ground level, while the negative values in the atmosphere and at the TOA

331 indicate an overall cooling effect at these higher altitudes.

332
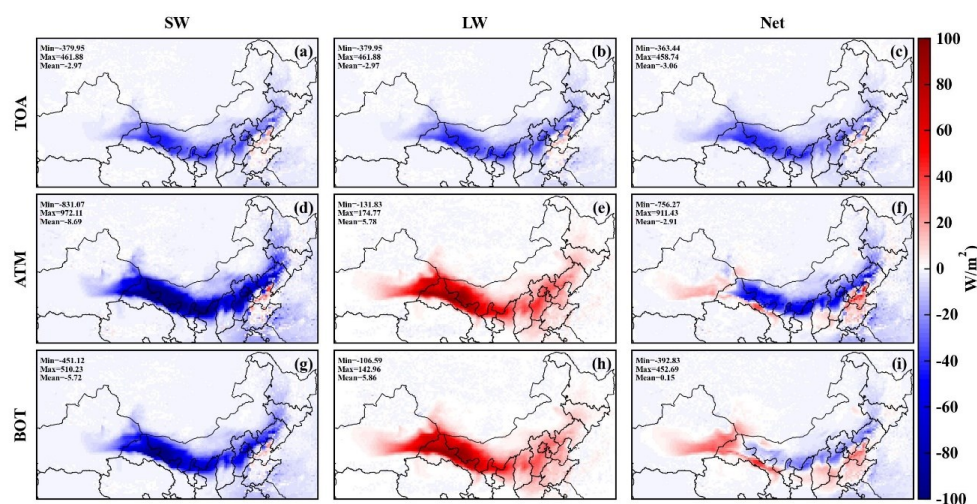
333

334   Figure 4. Radiation forcings due to bulk dust enabling ARI effects.

335

336   To assess the impact of dust mineralogical composition on radiative forcings, Figure

337   S6 illustrates the spatial distribution of radiative differences, considering the ARI effects

338   of bulk dust and comparing them to the default N2012 mineralogy atlas. This comparison

339   provides valuable insights into how variations in the mineralogical composition of dust

340   particles can influence the energy balance in the atmosphere. Compared to the ARI effects

341   of bulk dust, the mineralogical composition of dust aerosols can lead to increases in SW

342   radiation forcings at the surface and in the atmosphere, ranging from +0.10 to +0.82 $\mathrm{W\,m^{-2}}$.

343   This increase reflects the different optical properties of dust mineral types, which can affect

344   the scattering and absorption of solar radiation. These variations in the SW radiation

345   forcings are particularly important for understanding how different dust types modulate the

346   amount of solar radiation reaching the Earth's surface and atmosphere. At the TOA,

347   however, the mineralogical composition resulted in a decrease of about −0.72 $\mathrm{W\,m^{-2}}$ in

348   SW radiation forcing, suggesting that certain mineralogical types may be more efficient at

349   reflecting solar radiation back into space. Similar to SW radiation forcings, net radiation

350   forcings at the surface and in the atmosphere increased, ranging from +0.02 to +0.63 W

351   m^{-2}, while at the TOA, net radiation forcings decreased by about -0.65 W m^{-2}. The increase

352   in net radiation at the surface and in the atmosphere reflects the combined effect of

353   increased SW absorption and the potential changes in longwave (LW) radiative properties.

354   For LW radiation forcings, the mineralogical composition of dust led to decreases in the

355   radiative forcing across different layers, ranging from -0.72 to -0.12 W m^{-2}. This decrease

356   suggests that certain dust mineral types are more efficient at absorbing and emitting

357   longwave radiation, which can contribute to cooling effects in the atmosphere and at the

358   surface.

359
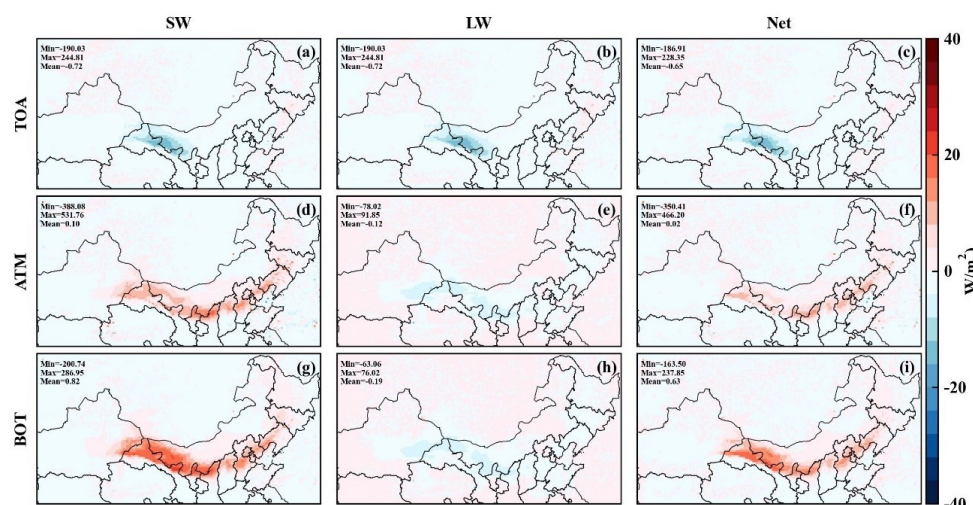
361   Figure 5. Difference between TOA, ATM and BOT radiation forcings with considering bulk dust and
362   mineralogical dust compositions (i.e., N2012_default) enabling ARI effects.

363

364   As demonstrated in Figure A3, the selection of the soil mineralogy dataset and the

365   modeling approach significantly influences the calculated dust radiative forcings. When

366   comparing shortwave dust radiative effects (DRE) from WRF-CHIMERE simulations

367   using the default N2012 and J2014 mineral atlases, we observe a minor discrepancy in the

368   DRE amplitude, particularly for shortwave and net radiation forcing at the surface. This

369   discrepancy suggests that the choice of mineralogical dataset can influence the magnitude

370   of radiative forcings, especially under varying atmospheric conditions. Previous research

371   has highlighted the distinct optical properties of hematite and goethite in the shortwave

372   spectrum (Lafon et al., 2006; Sokolik and Toon, 1999). These differences contribute to

373   variations in the dust's radiative properties and, in turn, its effect on energy transfer in the

374   atmosphere. Incorporating both minerals in dust production results in a flatter spectral

375   single scattering albedo (SSA), as goethite's less pronounced dependence on shortwave

376   wavelengths reduces the overall absorption in the shortwave spectrum (Formenti et al.,

377   2014). This effect is particularly noticeable when comparing the radiative forcings from

378   the different mineralogy datasets, as the presence of goethite alters the absorption and

379   scattering characteristics of the dust particles.

380   As depicted in Figure 6, the distinct day-night variations in shortwave radiation

381   forcing (SWRF) induced by ARI effects have been thoroughly demonstrated when

382   considering different mineralogical atlases compared to bulk dust. These variations reflect

383   the different impacts that dust aerosols have on solar radiation during the day and night,

384   with a clear difference in the magnitude of the effects between the two periods. Notably,

385   SWRF variations were more pronounced during the daytime than at night, which can be

386   attributed to the stronger interaction between dust aerosols and incoming solar radiation

387   during daylight hours. The presence of dust aerosols alters the reflection, absorption, and

388   scattering of sunlight, leading to significant changes in the radiation balance, especially

389   during the day when solar energy is at its peak.

390   Incorporating default dust mineralogical compositions into the simulations led to an

391   increase in daytime SWRF at the surface and within the atmosphere, ranging from 1.60 to

392   3.74 W m^{-2}. This increase suggests that the specific mineralogy of dust aerosols contributes

393   to greater absorption and scattering of solar radiation, amplifying the cooling effect at the

394   surface and the atmosphere. However, at the top of the atmosphere (TOA), the SWRF

395   decreased by approximately 2.00 W m^{-2}, which could be indicative of increased reflection

396   of shortwave radiation back into space due to the dust particles' optical properties. This

397   shift in radiative forcing at the TOA highlights the role of dust in altering the energy fluxes

398   across different atmospheric layers.

399   When comparing simulations using default dust mineralogical compositions to those

400   employing Earth-observing EMIT satellite data within the WRF-CHIMERE model,

401   notable differences in SWRF were observed. Daytime SWRF at the surface was reduced

402   for the N2012 mineralogy dataset (-1.88 W m^{-2}) and J2014 mineralogy dataset (-1.37 W

403   m^{-2}) when using EMIT data, compared to the default dust mineralogy compositions. This

404   reduction could be due to more accurate mineralogical characterization, which alters the

405   dust's optical properties and reduces its ability to absorb and scatter sunlight. Conversely,

406   SWRF was enhanced in the atmosphere (N2012: $+1.44$ W m^{-2}, J2014: $+0.84$ W m^{-2}) when

407   using the EMIT data, indicating that the updated mineralogical information leads to a

408   different interaction with solar radiation in the atmospheric layer, possibly due to changes

409   in dust composition that affect scattering and absorption properties at higher altitudes.

410   Furthermore, SWRF at the TOA transitioned from negative to positive in simulations

411   using the EMIT data. For the N2012 dataset, the SWRF varied from -1.73 to $+1.59$ W m^{-2},

412   and for the J2014 dataset, it ranged from -2.14 to $+0.07$ W m^{-2}. This shift suggests that

413   more accurate dust mineralogy data, particularly from satellite observations, can have a

414   significant impact on the amount of solar radiation reflected back to space, thereby

415   influencing the radiative balance at the TOA. The transition from negative to positive

416   forcing at the TOA emphasizes the importance of incorporating realistic mineralogical

417   information to enhance the accuracy of dust-related radiative forcing calculations and

418   better understand their role in climate systems.
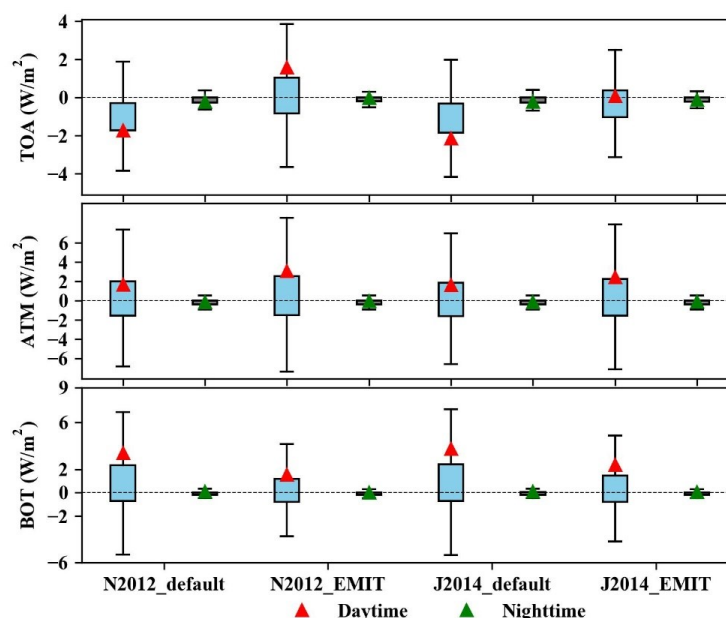
419

Figure 6. Day-night changes of TOA, ATM and BOT shortwave radiation forcings from simulations using different composition atlases (N2012_default, N2012_EMIT, J2014_default and J2014_EMIT) compared to bulk dust.

3.3 Radiative effect on air quality

Aerosol effects not only gave rise to changes in meteorological variables but also had a significant impact on air quality. As shown in Figure 7, the inclusion of bulk dust aerosol feedbacks in the WRF-CHIMERE model resulted in substantial increases in PM_{10} concentrations, with an average increase of 119.48 μg m⁻³. This rise in particulate matter highlights the important role of dust aerosols in contributing to local and regional air pollution, especially in regions that are susceptible to dust storms. Along with these increases in PM_{10} concentrations, O_3 concentrations slightly decreased, with an average reduction of −46.52 μg m⁻³. This reduction in ozone can be attributed to the complex interaction between dust particles and ozone precursor gases, where dust aerosols can act as both a sink for ozone and influence the photochemical processes that govern its formation and degradation.

The most pronounced increases in PM_{10} concentrations occurred in the Badain Jaran

438 Desert, a well-known dust source region, where peak values exceeded 1200 μg m⁻³. This

439 reflects the large dust emissions typical of desert environments, where strong winds

440 mobilize vast quantities of particulate matter. Downwind regions, including Ningxia,

441 Shaanxi, and Beijing, also experienced significant PM_{10} elevations, with concentration

442 differences reaching approximately 600 μg m⁻³ compared to baseline levels. These

443 increases in PM_{10} highlight the long-range transport of dust particles, which can impact air

444 quality far from the source regions and have implications for public health, especially in

445 urban areas.

446 While the use of speciated dust had some impact on long-range dust transport, its

447 overall effects on PM_{10} were relatively limited. The inclusion of more detailed

448 mineralogical data allowed for a better representation of dust composition but did not

449 significantly alter the overall dust load in terms of PM_{10} concentrations. This suggests that,

450 while dust speciation can influence the optical properties and radiative effects of dust, the

451 total mass concentration of dust particles in the atmosphere is primarily driven by factors

452 such as dust emission sources, atmospheric transport, and meteorological conditions, rather

453 than mineral composition alone.

454 Ozone changes along transport pathways were generally smaller than the surrounding

455 concentrations, typically ranging from −60 to −40 μg m⁻³. These smaller changes in O_3

456 concentrations reflect the fact that dust aerosols have a more localized and complex effect

457 on ozone formation and destruction, with significant variability depending on the regional

458 and temporal context. In particular, dust-induced reductions in ozone are likely to be

459 influenced by the local presence of other atmospheric constituents, such as nitrogen oxides

460 and volatile organic compounds, which play a key role in ozone chemistry.

461
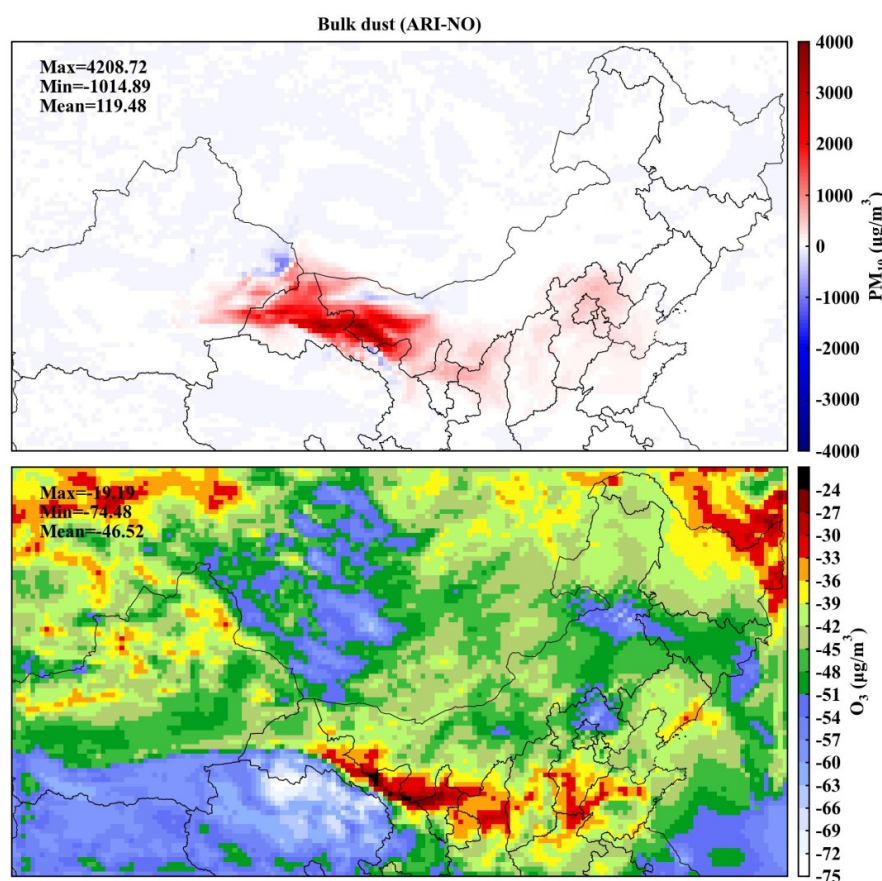
Figure 7. Changes in PM_{10} and O_3 concentrations resulting from bulk dust-induced ARI effects, compared to the scenario without aerosol feedbacks.

The spatial differences in PM_{10} and O_3 concentrations simulated by WRF-CHIMERE with different mineralogy atlases compared to bulk dust, enabling ARI effects, are depicted in Figures 8 and A4. These comparisons reveal substantial changes in the PM_{10} and O_3 concentrations across the different mineralogical compositions, including N2012_Default, N2012_EMIT, J2014_Default, J2014_EMIT, and bulk dust. This suggests that the normalization of the 12 minerals from these atlases significantly modifies meteorological conditions, further influencing the relative abundances of dust particles and their subsequent effects on air quality and atmospheric composition.

474   When compared to bulk dust, reduced PM_{10} concentrations were primarily observed

475   in the Taklimakan Desert, with decreases of around 60 μg m^{-3}, while increases in PM_{10}

476   concentrations occurred in the Badain Jaran Desert and its downwind regions, with

477   concentrations rising up to 1000 μg m^{-3}. These regional variations indicate that different

478   dust mineralogical compositions can impact the emission and transport of dust, with certain

479   mineral types leading to more efficient scattering or absorption of radiation, which may

480   alter the local meteorological conditions and dust dispersion patterns.

481   For O_3 concentrations, reductions and enhancements were mainly observed in the

482   Horqin sandy land and North China Plain, with changes up to 4 μg m^{-3}, respectively. This

483   highlights the complex interaction between dust aerosols and ozone chemistry, where dust

484   can either enhance or reduce ozone concentrations depending on the region. Dust aerosols

485   can influence ozone levels by acting as a surface for heterogeneous chemical reactions or

486   by modifying the photochemical processes that control ozone formation and destruction.

487   When considering the EMIT data, PM_{10} concentrations were reduced in dust source

488   regions and enhanced in downwind regions, with reductions of up to −1567.16 μg m^{-3} and

489   increases of +218.26 μg m^{-3}. This suggests that more accurate mineralogical data can

490   influence dust transport patterns, leading to greater reductions in PM_{10} at the source regions

491   and increased dust concentrations in the downwind areas. These findings further emphasize

492   the role of mineralogical composition in modulating dust aerosol behavior and distribution.

493   For O_3, enhancements appeared in source regions, while reductions were observed in

494   downwind regions, with changes ranging from −2.46 to +3.52 μg m^{-3}. These trends suggest

495   that more accurate dust speciation can influence regional ozone levels in different ways,

496   with possible implications for local air quality and atmospheric chemistry. Notably, the

497   impacts on PM_{10} concentrations from N2012_EMIT compared to N2012_Default were

498   larger than those observed from J2014_EMIT versus J2014_Default, while the impacts on

499   O_3 concentrations followed the opposite trends. This indicates that the choice of dust

500   mineralogical dataset has a differential impact on PM_{10} and O_3 concentrations,

501   underscoring the importance of considering mineral composition in aerosol modeling to

502   more accurately predict air quality and climate effects.

503
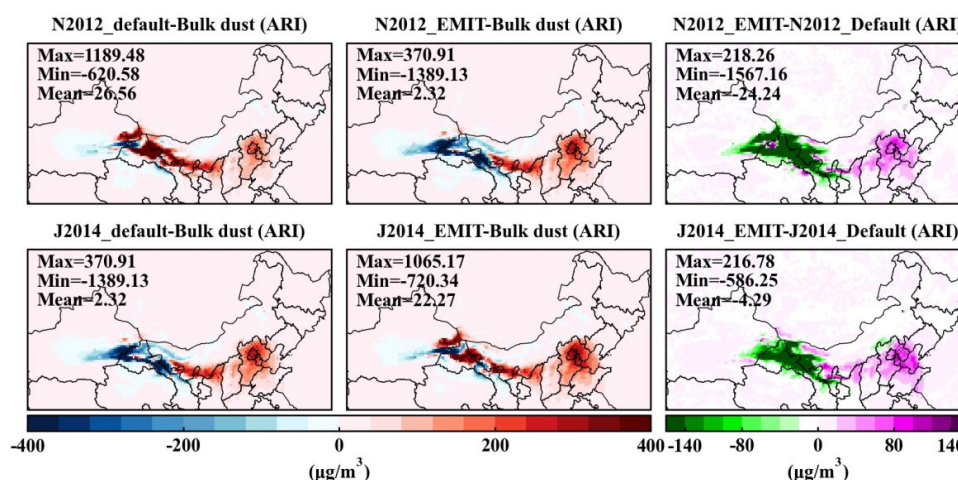
504

505   Figure 8. Difference in PM_{10} concentrations considering bulk dust and various dust mineralogy atlases
506   that enable ARI effects.

507

508   Figure 9 shows the percentage changes in surface concentrations of mineral dust with

509   and without considering ARI effects. These results provide valuable insight into how the

510   inclusion of ARI effects modifies the composition and radiative properties of dust aerosols,

511   depending on the mineralogical dataset used. For the N2012_default and N2012_EMIT

512   data, quartz and feldspar accounted for a substantial portion of the total dust, ranging from

513   approximately 51.7% to 57.4% for quartz and 18.6% to 19.8% for feldspar. This indicates

514   that quartz and feldspar are the dominant mineral components in the dust modeled with the

515   N2012 dataset.

516   In contrast, for the J2014_default dataset, the mineral composition was more

517   diversified, with calcite, quartz, and mica contributing about 26.3%, 24.0%, and 20.0%,

518   respectively, to the total dust composition. This shift in mineral proportions reflects the

519   differences in the mineralogical characterization between the N2012 and J2014 datasets,

520   with J2014 incorporating a broader range of dust minerals. For J2014_EMIT, the mineral

521 composition shifted further, with quartz and mica making up approximately 46.8% and

522 27.5% of the dust, respectively. This highlights the importance of using accurate

523 mineralogical data, such as that from EMIT satellite observations, to better represent the

524 composition of dust aerosols in simulations.

525 The inclusion of EMIT data led to an increase in the absorption percentage of hematite

526 by about 8% for N2012 and 6% for J2014. Hematite is a highly absorbing mineral,

527 especially in the shortwave spectrum, and its increased presence enhances the dust's ability

528 to absorb solar radiation, thereby affecting the DRE in the shortwave spectrum. This

529 increase in hematite absorption is significant, as it directly impacts the radiative effects of

530 dust, potentially contributing to a greater cooling effect on the atmosphere by modifying

531 the shortwave radiation balance.

532 While quartz constitutes the largest portion of the dust in both the N2012 and J2014

533 datasets, its DRF effects are relatively limited, as noted in Li et al. (2021). Quartz is known

534 for its high reflectivity in the shortwave spectrum, and while it makes up a large fraction

535 of the total dust mass, it has a less pronounced effect on radiative forcing compared to more

536 absorbing minerals like hematite or mica. This suggests that, despite its dominance in dust

537 composition, quartz plays a smaller role in modifying the energy balance of the atmosphere
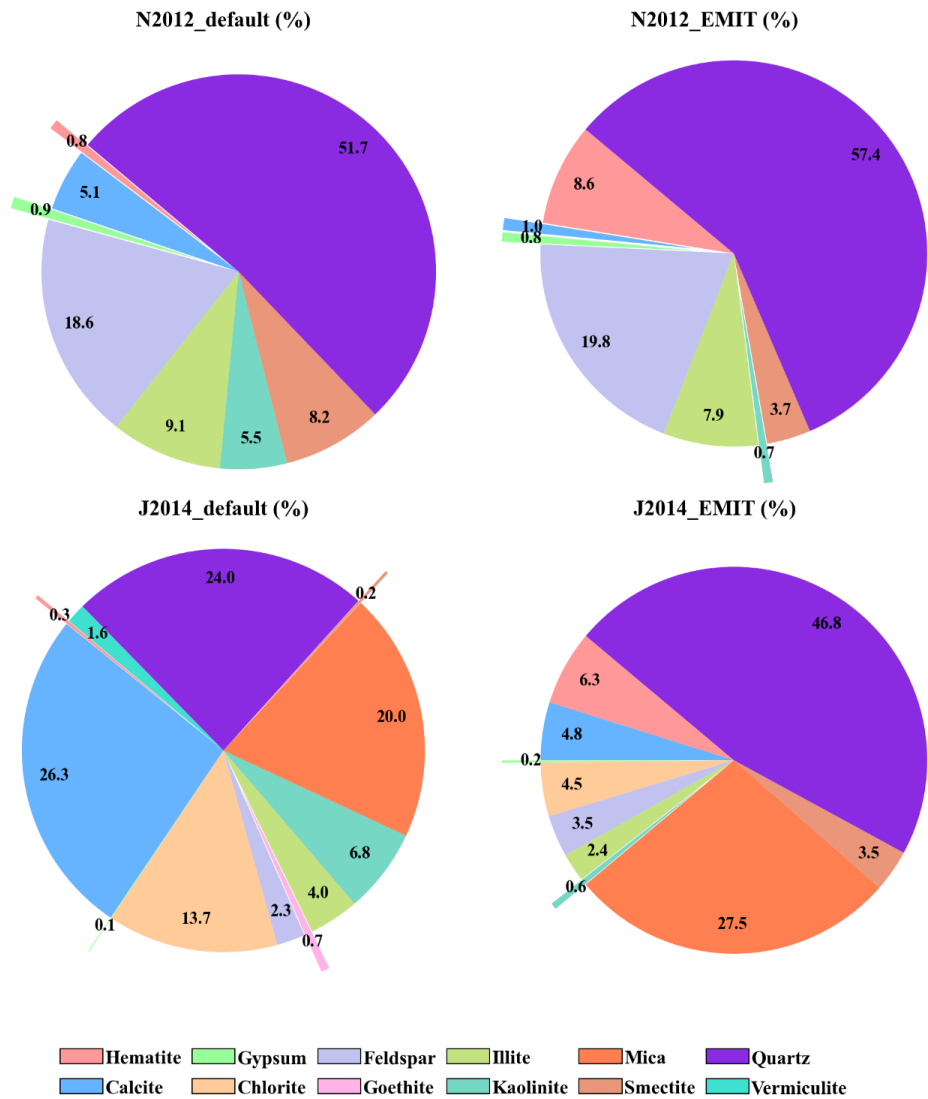
538 through direct radiative effects.

539

540

Figure 9. Contributions of different mineralogical compositions using N2012_default, N2012_EMIT, J2014_default, and J2014_EMIT, considering ARI effects, compared to the scenario without enabling aerosol feedbacks.

3.4 Limitations and uncertainties for aerosol feedbacks of mineralogical dust

The accuracy of simulated dust emission is intricately linked to soil properties, such as soil texture and moisture, which primarily influence the threshold friction velocity required for dust particle mobilization (Kim and Choi, 2015; Su and Fung, 2015). These

550 factors play a critical role in determining the magnitude and spatial distribution of dust

551 emissions, underscoring the need for precise and high-resolution soil data in dust modeling.

552 While the current EMIT L3 data offers a spatial resolution of $0.5° \times 0.5°$, real-time higher

553 spatial resolution datasets, such as the 60 m × 60 m EMIT L2B mineral atlas

554 (https://earth.jpl.nasa.gov/emit/internal_resources/282), can provide a more detailed

555 representation of soil mineralogy, thereby enhancing the fidelity of dust emission

556 simulations.

557   The uncertainty associated with dust mineralogical datasets is being actively

558 addressed by NASA's EMIT. This initiative has deployed a hyperspectral imaging

559 spectrometer aboard the International Space Station to deliver global retrievals of soil

560 mineral compositions with unprecedented spatial detail. The spectrometer captures spectral

561 absorption features within the UV to near-infrared range (0.38–2.5 μm), offering critical

562 insights into the distribution and variability of soil minerals (Castellanos et al., 2024;

563 Connelly et al., 2021). In addition to satellite-based observations, ground-based stations

564 play a vital role in measuring dust mineralogical compositions using stationary instruments,

565 which provide localized and highly accurate data. Complementing these measurements,

566 aircraft-based instruments offer the capability to sample dust particles along specific flight

567 tracks, providing valuable vertical and spatial profiles of speciated dust properties (e.g.,

568 size and mixing state, Panta et al., 2023; Ryder et al., 2015). Together, these observational

569 platforms form a robust foundation for validating and improving dust models.

570   Aerosol-cloud interactions involving speciated dust are another critical aspect of dust-

571 climate interactions that require further investigation, especially for feldspar and quartz

572 (Atkinson et al., 2013; Chatziparaschos et al., 2023). Incorporating these interactions into

573 two-way coupled WRF-CHIMERE models can provide a more comprehensive

574 understanding of the feedback mechanisms between dust aerosols and cloud microphysics.

575 Such implementations are currently a focus of ongoing work, aiming to refine the

576 representation of dust-induced radiative and microphysical effects in regional and global

577   models. These efforts will not only improve model accuracy but also enhance our ability

578   to predict the impacts of dust on weather, air quality, and climate.

579

580   **4 Conclusion**

581   This study has provided a comprehensive analysis of the role of dust mineral

582   composition in atmospheric radiation and pollution in North China, using a two-way

583   coupled WRF-CHIMERE model integrated with three mineralogical datasets (N2012,

584   J2014, and L2024 from EMIT). The research focused on the March 2021 dust storm event

585   to evaluate the ARI effects and their impacts on regional meteorology and air quality.

586   The findings revealed significant spatial variations in radiative forcing due to

587   differences in dust mineralogy. Compared to the ARI effects of bulk dust, the mineralogical

588   composition of dust aerosols can increase SW radiation forcing at the surface and in the

589   atmosphere by +0.10 to +0.82 W m^{-2}, while simultaneously causing a decrease of

590   approximately −0.72 W m^{-2} in SW radiation forcing at the TOA. Integrating EMIT data

591   into the model reduced PM$_{10}$ biases by over 15% in high-concentration regions and

592   improved ozone predictions, with localized changes ranging from −2.46 to +3.52 µg m^{-3}.

593   Specifically, the ARI effects of these mineralogical compositions led to a notable increase

594   in PM$_{10}$ levels, reaching up to 1189.48 µg m^{-3} in dust source regions, when compared to

595   bulk dust scenarios.

596   These findings highlight the critical importance of considering mineralogical data in

597   improving simulations of dust-related radiative forcing and air quality impacts. High-

598   resolution observational data, such as EMIT satellite observations, combined with

599   sensitivity studies that account for a wider range of observational factors, including

600   atmospheric conditions under varying aerosol optical depth and water vapor loading, as

601   well as the spectral representation of surface mineralogical features, along with alternative

602   parameterizations of instrument noise of variable signal-to-noise and spectral sampling or

603   entirely different mineral identification algorithms, are crucial for improving atmospheric

604   models for dust simulations. Additionally, this study emphasizes the need for a more

605　nuanced understanding of the feedback mechanisms between dust mineral composition and

606　cloud microphysics, which can significantly influence regional climate dynamics and air

607　quality.

608　　　Despite the robust methodology and comprehensive analysis, several limitations are

609　acknowledged. The model exhibited systematic biases in simulating surface radiation

610　fluxes, near-surface wind dynamics, and temperature fields, particularly in North China.

611　These biases suggest challenges in accurately capturing the complex interactions between

612　dust aerosols and the atmosphere. The choice of mineralogical datasets and modeling

613　framework also significantly affected the calculated dust radiative forcings, indicating a

614　need for further refinement and validation of these datasets.

615　　　Future research should focus on integrating aerosol-cloud interactions of speciated

616　dust into two-way coupled models to enhance our understanding of feedback mechanisms

617　between dust aerosols and cloud microphysics. Furthermore, the development and

618　incorporation of higher-resolution soil data and real-time satellite observations could

619　further refine dust emission simulations and reduce model biases.

620

621　**Data and software availability**

622　　　The meteorological ICs and BCs, Chemical ICs and BCs and emission data used for

623　WRF–CHIMERE and all data used to create figures and tables in this study are provided

624　in an open repository on Zenodo (https://doi.org/10.5281/zenodo.14728874, Gao et al.,

625　2025a). Himawari and CALIPSO satellite data are available at

626　ftp://ftp.ptree.jaxa.jp/jma/netcdf and https://subset.larc.nasa.gov/calipso, respectively.

627　　　The source codes of the two-way coupled WRFv3.7.1–CHIMERE v2020r3 models

628　are obtained from https://www.lmd.polytechnique.fr/chimere. The related source codes,

629　configuration information, namelist files and automated run scripts of these three two-way

630　coupled models are archived at Zenodo with the following associated DOI:

631　https://doi.org/10.5281/zenodo.14729124 (Gao et al., 2025b).

632

Author contributions

633

634   CG, XZ, HY and LH carried out the data collection, related analysis, figure plotting,

635   and paper writing. HZ, SZ, and AX were involved with the original research plan and made

636   suggestions for the paper writing.

637   **Competing interests**

638   The contact author has declared that neither they nor their co-authors have any

639   competing interests.

640

641   **Acknowledgments**

650

651   **Reference**

652   Adebiyi, A., Kok, J. F., Murray, B. J., Ryder, C. L., Stuut, J.-B. W., Kahn, R. A., Knippertz, P., Formenti,
653   P., Mahowald, N. M., and García-Pando, C. P.: A review of coarse mineral dust in the Earth
654   system, Aeolian Research, 60, 100849, https://doi.org/10.1016/j.aeolia.2022.100849, 2023.
655   Alfaro, S., Lafon, S., Rajot, J., Formenti, P., Gaudichet, A., and Maille, M.: Iron oxides and light
656   absorption by pure desert dust: An experimental study, Journal of Geophysical Research:
657   Atmospheres, 109, https://doi.org/10.1029/2003JD004374, 2004.
658   Atkinson, J. D., Murray, B. J., Woodhouse, M. T., Whale, T. F., Baustian, K. J., Carslaw, K. S., Dobbie,
659   S., O'Sullivan, D., and Malkin, T. L.: The importance of feldspar for ice nucleation by mineral
660   dust in mixed-phase clouds, Nature, 498, 355–358, https://doi.org/10.1038/nature12278, 2013.
661   Balkanski, Y., Bonnet, R., Boucher, O., Checa-Garcia, R., and Servonnat, J.: Better representation of
662   dust can improve climate models with too weak an African monsoon, Atmospheric Chemistry
663   and Physics, 21, 11423–11435, https://doi.org/10.5194/acp-21-11423-2021, 2021.
664   Briant, R., Tuccella, P., Deroubaix, A., Khvorostyanov, D., Menut, L., Mailler, S., and Turquety, S.:
665   Aerosol–radiation interaction modelling using online coupling between the WRF 3.7.1
666   meteorological model and the CHIMERE 2016 chemistry-transport model, through the

667   OASIS3-MCT coupler, Geosci. Model Dev., 10, 927–944, https://doi.org/10.5194/gmd-10-
668   927-2017, 2017.

669   Castellanos, P., Colarco, P., Espinosa, W. R., Guzewich, S. D., Levy, R. C., Miller, R. L., Chin, M., Kahn,
670   R. A., Kemppinen, O., and Moosmüller, H.: Mineral dust optical properties for remote sensing
671   and global modeling: A review, Remote Sensing of Environment, 303, 113982,
672   https://doi.org/10.1016/j.rse.2023.113982, 2024.

673   Chatziparaschos, M., Daskalakis, N., Myriokefalitakis, S., Kalivitis, N., Nenes, A., Gonçalves Ageitos,
674   M., Costa-Surós, M., Pérez García-Pando, C., Zanoli, M., Vrekoussis, M., and Kanakidou, M.:
675   Role of K-feldspar and quartz in global ice nucleation by mineral dust in mixed-phase clouds,
676   Atmos. Chem. Phys., 23, 1785–1801, https://doi.org/10.5194/acp-23-1785-2023, 2023.

677   Choobari, O. A., Zawar-Reza, P., and Sturman, A.: The global distribution of mineral dust and its
678   impacts on the climate system: A review, Atmospheric Research, 138, 152–165,
679   https://doi.org/10.1016/j.atmosres.2013.11.007, 2014.

680   Claquin, T., Schulz, M., and Balkanski, Y.: Modeling the mineralogy of atmospheric dust sources,
681   Journal of Geophysical Research: Atmospheres, 104, 22243–22256,
682   https://doi.org/10.1029/1999JD900416, 1999.

683   Connelly, D. S., Thompson, D. R., Mahowald, N. M., Li, L., Carmon, N., Okin, G. S., and Green, R. O.:
684   The EMIT mission information yield for mineral dust radiative forcing, Remote Sensing of
685   Environment, 258, 112380, https://doi.org/10.1016/j.rse.2021.112380, 2021.

686   Cwiertny, D. M., Young, M. A., and Grassian, V. H.: Chemistry and photochemistry of mineral dust
687   aerosol, Annu. Rev. Phys. Chem., 59, 27–51,
688   https://doi.org/10.1146/annurev.physchem.59.032607.093630, 2008.

689   Duniway, M. C., Pfennigwerth, A. A., Fick, S. E., Nauman, T. W., Belnap, J., and Barger, N. N.: Wind
690   erosion and dust from US drylands: a review of causes, consequences, and solutions in a
691   changing world, Ecosphere, 10, e02650, https://doi.org/10.1002/ecs2.2650, 2019.

692   Fécan, F., Marticorena, B., and Bergametti, G.: Parametrization of the increase of the aeolian erosion
693   threshold wind friction velocity due to soil moisture for arid and semi-arid areas, Annales
694   Geophysicae, 17, 149–157, https://doi.org/10.1007/s00585-999-0149-7, 1998.

695   Formenti, P., Caquineau, S., Desboeufs, K., Klaver, A., Chevaillier, S., Journet, E., and Rajot, J.-L.:
696   Mapping the physico-chemical properties of mineral dust in western Africa: mineralogical
697   composition, Atmospheric Chemistry and Physics, 14, 10663–10686,
698   https://doi.org/10.5194/acp-14-10663-2014, 2014.

699   Gao, C., Xiu, A., Zhang, X., Tong, Q., Zhao, H., Zhang, S., Yang, G., and Zhang, M.: Two-way coupled
700   meteorology and air quality models in Asia: a systematic review and meta-analysis of impacts
701   of aerosol feedbacks on meteorology and air quality, Atmos. Chem. Phys., 22, 5265–5329,
702   https://doi.org/10.5194/acp-22-5265-2022, 2022.

703   Gómez Maqueo Anaya, S., Althausen, D., Faust, M., Baars, H., Heinold, B., Hofer, J., Tegen, I.,
704   Ansmann, A., Engelmann, R., and Skupin, A.: The implementation of dust mineralogy in
705   COSMO5. 05-MUSCAT, Geoscientific Model Development, 17, 1271–1295,
706   https://doi.org/10.5194/gmd-17-1271-2024, 2024.

707   Gonçalves Ageitos, M., Obiso, V., Miller, R. L., Jorba, O., Klose, M., Dawson, M., Balkanski, Y.,

708   Perlwitz, J., Basart, S., Di Tomaso, E., Escribano, J., Macchia, F., Montané, G., Mahowald, N.
709   M., Green, R. O., Thompson, D. R., and Pérez García-Pando, C.: Modeling dust mineralogical
710   composition: sensitivity to soil mineralogy atlases and their expected climate impacts, Atmos.
711   Chem. Phys., 23, 8623–8657, https://doi.org/10.5194/acp-23-8623-2023, 2023.

712 Green, R. O., Mahowald, N., Ung, C., Thompson, D. R., Bator, L., Bennet, M., Bernas, M., Blackway,
713   N., Bradley, C., and Cha, J.: The Earth surface mineral dust source investigation: An Earth
714   science imaging spectroscopy mission, 2020 IEEE aerospace conference, 1–15, 2020.

715 Harrison, A. D., Whale, T. F., Carpenter, M. A., Holden, M. A., Neve, L., O'Sullivan, D., Vergara
716   Temprado, J., and Murray, B. J.: Not all feldspars are equal: a survey of ice nucleating
717   propertiesacross the feldspar group of minerals, Atmos. Chem. Phys., 16, 10927–10940,
718   https://doi.org/10.5194/acp-16-10927-2016, 2016.

719 Journet, E., Balkanski, Y., and Harrison, S. P.: A new data set of soil mineralogy for dust-cycle modeling,
720   Atmos. Chem. Phys., 14, 3801–3816, https://doi.org/10.5194/acp-14-3801-2014, 2014.

721 Ke, Z., Liu, X., Wu, M., Shan, Y., and Shi, Y.: Improved dust representation and impacts on dust
722   transport and radiative effect in CAM5, Journal of Advances in Modeling Earth Systems, 14,
723   e2021MS002845, https://doi.org/10.1029/2021MS002845, 2022.

724 Kim, H. and Choi, M.: Impact of soil moisture on dust outbreaks in East Asia: Using satellite and
725   assimilation data, Geophysical Research Letters, 42, 2789–2796,
726   https://doi.org/10.1002/2015GL063325, 2015.

727 Klingmüller, K., Lelieveld, J., Karydis, V. A., and Stenchikov, G. L.: Direct radiative effect of dust–
728   pollution interactions, Atmospheric Chemistry and Physics, 19, 7397–7408,
729   https://doi.org/10.5194/acp-19-7397-2019, 2019.

730 Kok, J., Mahowald, N., Fratini, G., Gillies, J., Ishizuka, M., Leys, J., Mikami, M., Park, M.-S., Park, S.-
731   U., and Van Pelt, R.: An improved dust emission model–Part 1: Model description and
732   comparison against measurements, Atmospheric Chemistry and Physics, 14, 13023–13041,
733   https://doi.org/10.5194/acp-14-13023-2014, 2014.

734 Kok, J. F., Ridley, D. A., Zhou, Q., Miller, R. L., Zhao, C., Heald, C. L., Ward, D. S., Albani, S., and
735   Haustein, K.: Smaller desert dust cooling effect estimated from analysis of dust size and
736   abundance, Nature Geoscience, 10, 274–278, https://doi.org/10.1038/ngeo2912, 2017.

737 Kok, J. F., Storelvmo, T., Karydis, V. A., Adebiyi, A. A., Mahowald, N. M., Evan, A. T., He, C., and
738   Leung, D. M.: Mineral dust aerosol impacts on global climate and climate change, Nature
739   Reviews Earth & Environment, 4, 71–86, https://doi.org/10.1038/s43017-022-00379-5, 2023.

740 Kumar, A., Marcolli, C., Luo, B., and Peter, T.: Ice nucleation activity of silicates and aluminosilicates
741   in pure water and aqueous solutions–Part 1: The K-feldspar microcline, Atmospheric Chemistry
742   and Physics, 18, 7057–7079, https://doi.org/10.5194/acp-18-7057-2018, 2018.

743 Lafon, S., Sokolik, I. N., Rajot, J. L., Caquineau, S., and Gaudichet, A.: Characterization of iron oxides
744   in mineral dust aerosols: Implications for light absorption, Journal of Geophysical Research:
745   Atmospheres, 111, https://doi.org/10.1029/2005JD007016, 2006.

746 Li, L. and Sokolik, I. N.: The dust direct radiative impact and Its sensitivity to the land surface state and
747   key minerals in the WRF-Chem-DuMo Model: a case study of dust storms in Central Asia,
748   Journal of Geophysical Research: Atmospheres, 123, 4564–4582,

749   https://doi.org/10.1029/2017JD027667, 2018.

750   Li, L., Mahowald, N. M., Miller, R. L., Pérez García-Pando, C., Klose, M., Hamilton, D. S., Gonçalves
751   Ageitos, M., Ginoux, P., Balkanski, Y., Green, R. O., Kalashnikova, O., Kok, J. F., Obiso, V.,
752   Paynter, D., and Thompson, D. R.: Quantifying the range of the dust direct radiative effect due
753   to source mineralogy uncertainty, Atmos. Chem. Phys., 21, 3973–4005,
754   https://doi.org/10.5194/acp-21-3973-2021, 2021.

755   Li, L., Mahowald, N. M., Kok, J. F., Liu, X., Wu, M., Leung, D. M., Hamilton, D. S., Emmons, L. K.,
756   Huang, Y., Sexton, N., Meng, J., and Wan, J.: Importance of different parameterization changes
757   for the updated dust cycle modeling in the Community Atmosphere Model (version 6.1), Geosci.
758   Model Dev., 15, 8181–8219, https://doi.org/10.5194/gmd-15-8181-2022, 2022.

759   Li, L., Mahowald, N. M., Gonçalves Ageitos, M., Obiso, V., Miller, R. L., Pérez García-Pando, C., Di
760   Biagio, C., Formenti, P., Brodrick, P. G., and Clark, R. N.: Improved constraints on hematite
761   refractive index for estimating climatic effects of dust aerosols, Communications Earth &
762   Environment, 5, 295, https://doi.org/10.1038/s43247-024-01441-4, 2024.

763   Maher, B. A., Prospero, J. M., Mackie, D., Gaiero, D., Hesse, P. P., and Balkanski, Y.: Global
764   connections between aeolian dust, climate and ocean biogeochemistry at the present day and at
765   the last glacial maximum, Earth-Science Reviews, 99, 61–97,
766   https://doi.org/10.1016/j.earscirev.2009.12.001, 2010.

767   Menut, L., Siour, G., Bessagnet, B., Couvidat, F., Journet, E., Balkanski, Y., and Desboeufs, K.:
768   Modelling the mineralogical composition and solubility of mineral dust in the Mediterranean
769   area with CHIMERE 2017r4, Geosci. Model Dev., 13, 2051–2071,
770   https://doi.org/10.5194/gmd-13-2051-2020, 2020.

771   Nickovic, S., Vukovic, A., Vujadinovic, M., Djurdjevic, V., and Pejanovic, G.: Technical Note: High-
772   resolution mineralogical database of dust-productive soils for atmospheric dust modeling,
773   Atmos. Chem. Phys., 12, 845–855, https://doi.org/10.5194/acp-12-845-2012, 2012.

774   Obiso, V., Gonçalves Ageitos, M., Pérez García-Pando, C., Perlwitz, J. P., Schuster, G. L., Bauer, S. E.,
775   Di Biagio, C., Formenti, P., Tsigaridis, K., and Miller, R. L.: Observationally constrained
776   regional variations of shortwave absorption by iron oxides emphasize the cooling effect of dust,
777   Atmospheric Chemistry and Physics, 24, 5337–5367, https://doi.org/10.5194/acp-24-5337-
778   2024, 2024.

779   Panta, A., Kandler, K., Alastuey, A., González-Flórez, C., González-Romero, A., Klose, M., Querol, X.,
780   Reche, C., Yus-Díez, J., and Pérez García-Pando, C.: Insights into the single-particle
781   composition, size, mixing state, and aspect ratio of freshly emitted mineral dust from field
782   measurements in the Moroccan Sahara using electron microscopy, Atmospheric Chemistry and
783   Physics, 23, 3861–3885, https://doi.org/10.5194/acp-23-3861-2023, 2023.

784   Ryder, C., McQuaid, J. B., Flamant, C., Rosenberg, P., Washington, R., Brindley, H., Highwood, E.,
785   Marsham, J., Parker, D., and Todd, M.: Advances in understanding mineral dust and boundary
786   layer processes over the Sahara from Fennec aircraft observations, Atmospheric Chemistry and
787   Physics, 15, 8479–8520, https://doi.org/10.5194/acp-15-8479-2015, 2015.

788   Scanza, R. A., Mahowald, N., Ghan, S., Zender, C. S., Kok, J. F., Liu, X., Zhang, Y., and Albani, S.:
789   Modeling dust as component minerals in the Community Atmosphere Model: development of

790   framework and impact on radiative forcing, Atmos. Chem. Phys., 15, 537–561,
791   https://doi.org/10.5194/acp-15-537-2015, 2015.

792 Schepanski, K.: Transport of mineral dust and its impact on climate, Geosciences, 8, 151,
793   https://doi.org/10.3390/geosciences8050151, 2018.

794 Shao, Y. and Lu, H.: A simple expression for wind erosion threshold friction velocity, Journal of
795   Geophysical Research: Atmospheres, 105, 22437–22443,
796   https://doi.org/10.1029/2000JD900304, 2000.

797 Shao, Y., Wyrwoll, K.-H., Chappell, A., Huang, J., Lin, Z., McTainsh, G. H., Mikami, M., Tanaka, T. Y.,
798   Wang, X., and Yoon, S.: Dust cycle: An emerging core theme in Earth system science, Aeolian
799   Research, 2, 181–204, https://doi.org/10.1016/j.aeolia.2011.02.001, 2011.

800 Sokolik, I. N. and Toon, O. B.: Incorporation of mineralogical composition into models of the radiative
801   properties of mineral aerosol from UV to IR wavelengths, J. Geophys. Res., 104, 9423–9444,
802   https://doi.org/10.1029/1998JD200048, 1999.

803 Solomos, S., Spyrou, C., Bartsotas, N. S., Sykioti, O., Amiridis, V., Gkikas, A., Marinou, E., Katsafados,
804   P., Tsarpalis, K., and Pejanovic, G.: The Development of a Dust Mineralogy Map from Satellite
805   Retrievals and Implementation in WRF-Chem, Environmental Sciences Proceedings, 26, 54,
806   https://doi.org/10.3390/environsciproc2023026054, 2023a.

807 Solomos, S., Spyrou, C., Barreto, A., Rodríguez, S., González, Y., Neophytou, M. K., Mouzourides, P.,
808   Bartsotas, N. S., Kalogeri, C., and Nickovic, S.: The development of METAL-WRF Regional
809   Model for the Description of Dust Mineralogy in the Atmosphere, Atmosphere, 14, 1615,
810   https://doi.org/10.3390/atmos14111615, 2023b.

811 Song, Q., Ginoux, P., Gonçalves Ageitos, M., Miller, R. L., Obiso, V., and Pérez García-Pando, C.:
812   Modeling impacts of dust mineralogy on fast climate response, Atmospheric Chemistry and
813   Physics, 24, 7421–7446, https://doi.org/10.5194/acp-24-7421-2024, 2024.

814 Su, L. and Fung, J. C.: Sensitivities of WRF-Chem to dust emission schemes and land surface properties
815   in simulating dust cycles during springtime over East Asia, Journal of Geophysical Research:
816   Atmospheres, 120, 11–215, https://doi.org/10.1002/2015JD023446, 2015.

817 Swayze, G. A., Clark, R. N., Goetz, A. F., Chrien, T. G., and Gorelick, N. S.: Effects of spectrometer
818   band pass, sampling, and signal-to-noise ratio on spectral identification using the Tetracorder
819   algorithm, Journal of Geophysical Research: Planets, 108,
820   https://doi.org/10.1029/2002JE001975, 2003.

821 Tang, W., Yang, K., Qin, J., Li, X., and Niu, X.: A 16-year dataset (2000–2015) of high-resolution (3 h,
822   10 km) global surface solar radiation, Earth System Science Data, 11, 1905–1915,
823   https://doi.org/10.5194/essd-11-1905-2019, 2019.

824 Tong, D. Q., Gill, T. E., Sprigg, W. A., Van Pelt, R. S., Baklanov, A. A., Barker, B. M., Bell, J. E., Castillo,
825   J., Gassó, S., and Gaston, C. J.: Health and safety effects of airborne soil dust in the Americas
826   and beyond, Reviews of Geophysics, 61, e2021RG000763,
827   https://doi.org/10.1029/2021RG000763, 2023.

828 Tuccella, P., Menut, L., Briant, R., Deroubaix, A., Khvorostyanov, D., Mailler, S., Siour, G., and
829   Turquety, S.: Implementation of Aerosol-Cloud Interaction within WRF-CHIMERE Online
830   Coupled Model: Evaluation and Investigation of the Indirect Radiative Effect from

831   Anthropogenic Emission Reduction on the Benelux Union, Atmosphere, 10, 20,
832   https://doi.org/10.3390/atmos10010020, 2019.
833   Wang, X., Zhang, L., and Moran, M. D.: Development of a new semi-empirical parameterization for
834   below-cloud scavenging of size-resolved aerosol particles by both rain and snow, Geoscientific
835   Model Development, 7, 799–819, https://doi.org/10.5194/gmd-7-799-2014, 2014.
836   Willis, P. T. and Tattelman, P.: Drop-size distributions associated with intense rainfall, Journal of Applied
837   Meteorology   and   Climatology,   28,   3–15,   https://doi.org/10.1175/1520-
838   0450(1989)028<0003:DSDAWI>2.0.CO;2, 1989.
839   Zhang, L., Gong, S., Padro, J., and Barrie, L.: A size-segregated particle dry deposition scheme for an
840   atmospheric   aerosol   module,   Atmospheric   environment,   35,   549–560,
841   https://doi.org/10.1016/S1352-2310(00)00326-5, 2001.

842

843   **Appendix**

844   Table A1. Model setups and inputs for the WRF-CHIMERE model.

		WRF-CHIMERE
Domain configuration	Horizontal grid spacing	27 km (165 × 87)
	Vertical resolution	33 levels
Physics parameterization	Shortwave radiation	RRTMG
	Longwave radiation	RRTMG
	Cloud microphysics	Thompson
	PBL	YSU
	Cumulus	Grell-Freitas
	Surface	Monin-Obukhov
	Land surface	Noah LSM
	Icloud	Xu-Randall method
Chemistry scheme	Aerosol mechanism	SAM
	Aerosol size distribution	Sectional (10 bins)
	Aerosol mixing state	Core-Shell
	Gas-phase chemistry	MELCHIOR2
	Photolysis	Fast-JX with cloud effects
Emission	Dust emission	Kok
Input data	Meteorological ICs and BCs	FNL
	Chemical ICs and BCs	LMDZ-INCA

845

846
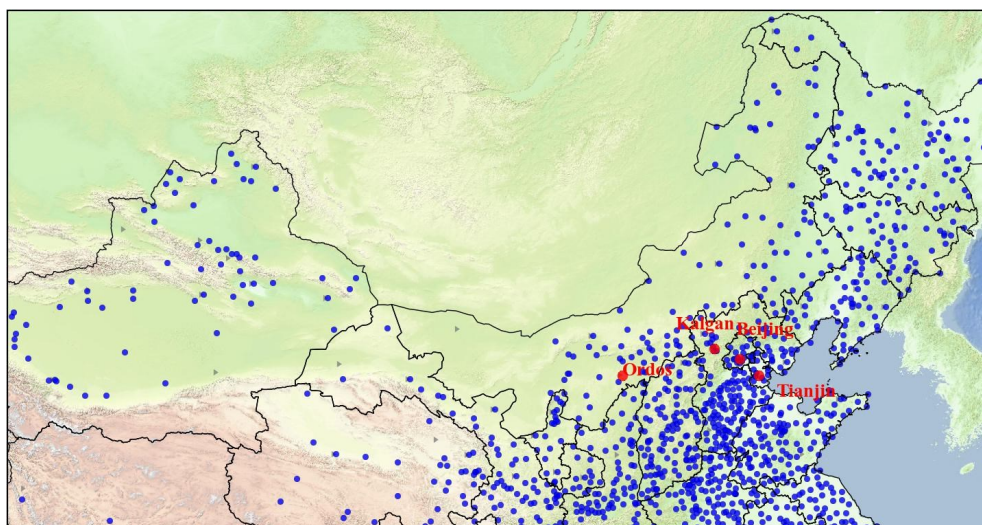
Figure A1. Simulation domain and locations of meteorology and air quality monitoring stations.
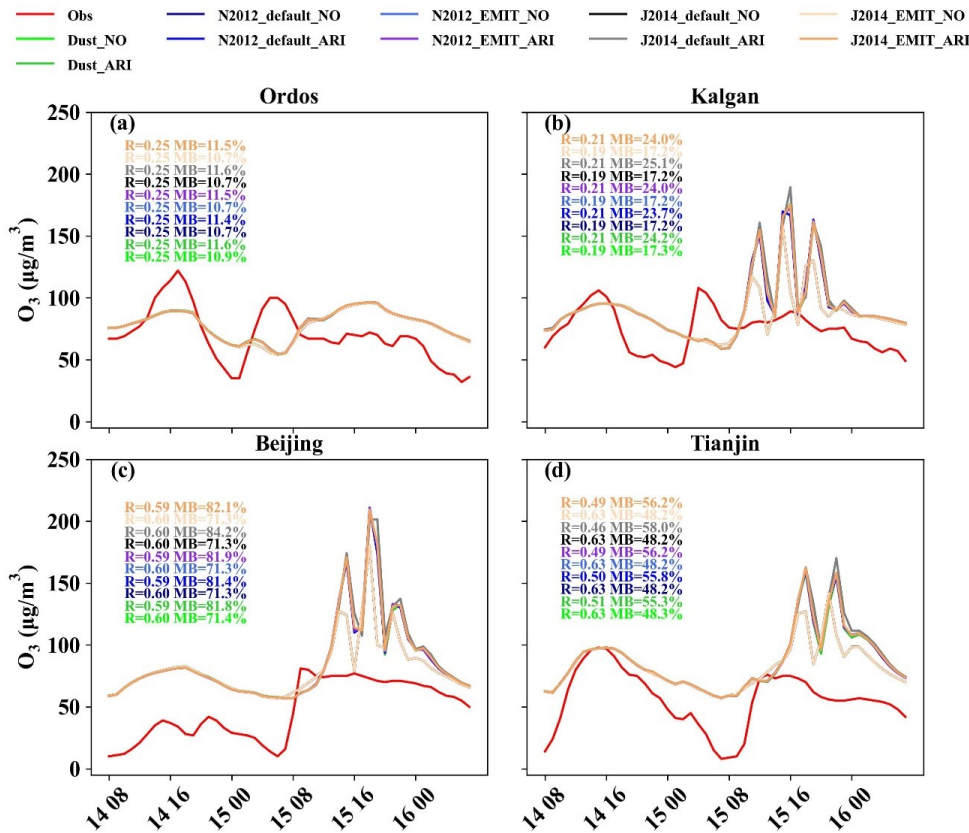
Figure A2. Statatiscal metrices between observed and simulated O_3 concentrations by different scenario simulations.
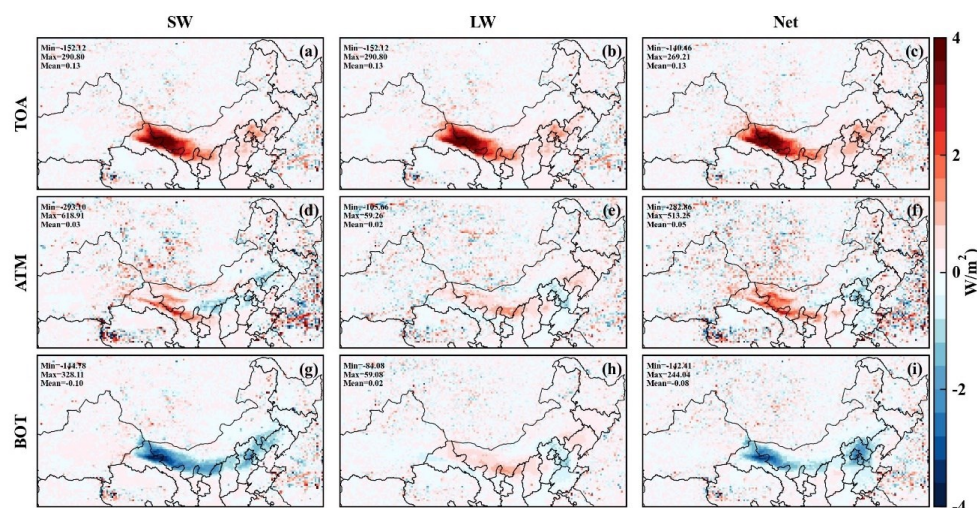
854

Figure A3. Difference between TOA, ATM and BOT radiation forcings with considering J2014 and
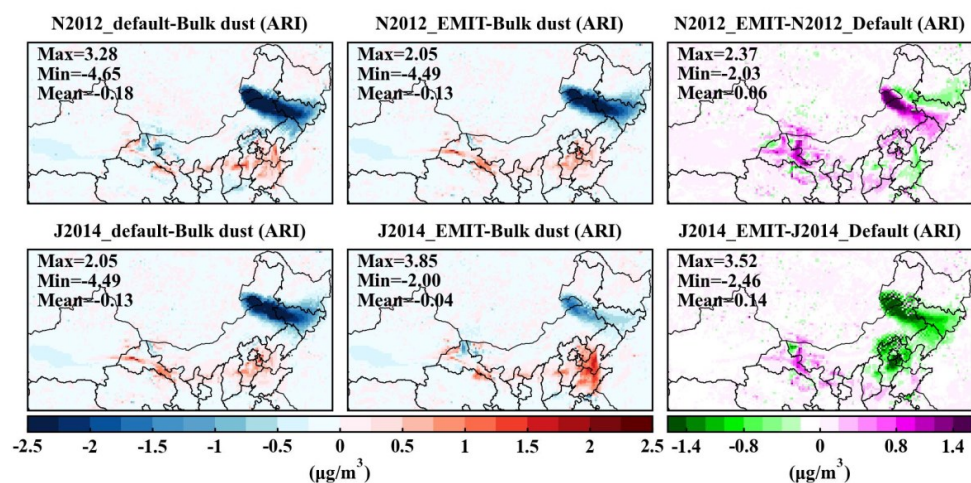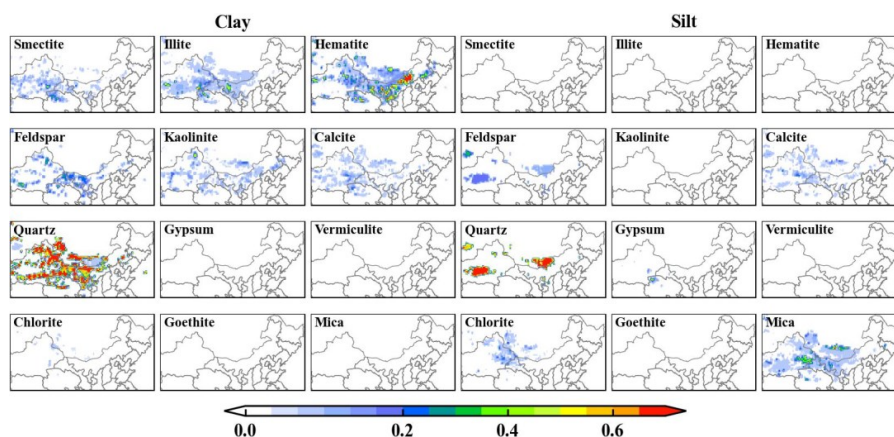N2012 mineralogical dust compositions (i.e., N2012_default) enabling ARI effects.

857

858

Figure A4. Difference in O$_3$ concentrations considering bulk dust and various dust mineralogy atlases
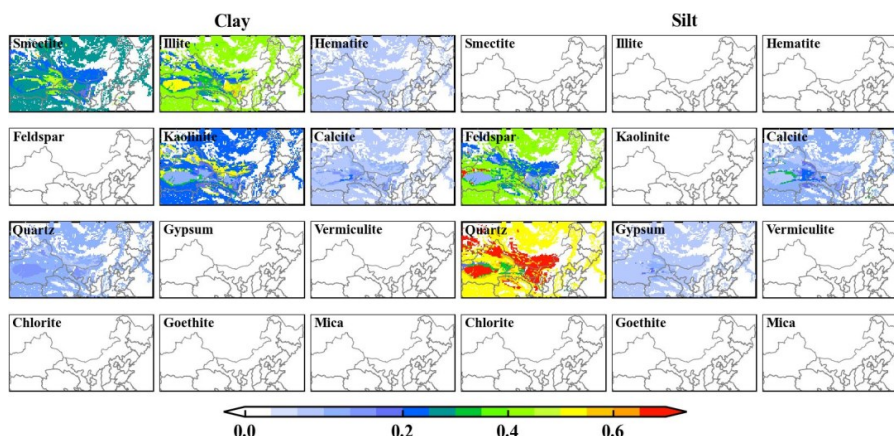that enable ARI effects.

861

862

Figure A5. Spatial distribution of content for the different mineral dust species in the silt and clay fraction of the soil for J2014 with EMIT satellite data.
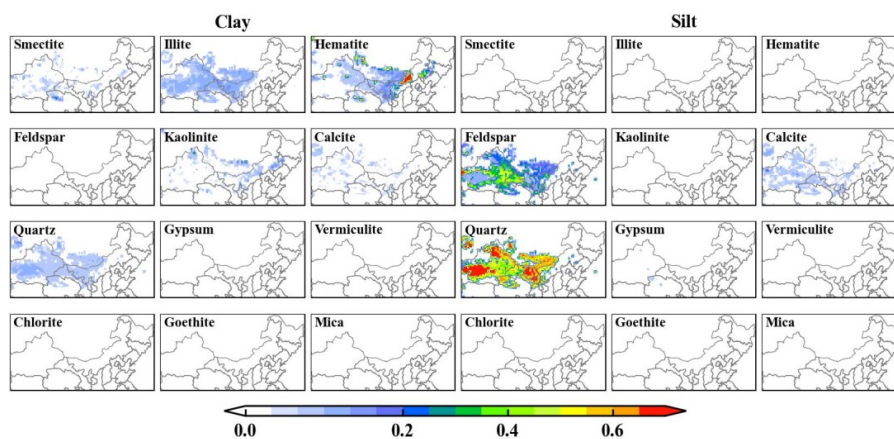

Figure A6. Spatial distribution of content for the different mineral dust species in the silt and clay fraction of the soil for original N2012 mineralogical data.

Figure A7. Spatial distribution of content for the different mineral dust species in the silt and clay fraction of the soil for N2012 with EMIT satellite data.